Journal of Superconductivity and Novel Magnetism (2022) 35:2987–2998
https://doi.org/10.1007/s10948-022-06322-5

ORIGINAL PAPER

Removal of Heavy Metal (Cadmium) Using Temperature Optimized Novel Rare Earth Garnet ($Y_3Fe_5O_{12}$) Through Simple, Robust, and Efficient Adsorption Technique

M. Asisi Janifer[1] · C. Joseph Prabagar[1] · M. Maria Lumina Sonia[1] · S. Pauline[1] · S. Anand[2] · P. Ranjini[3]

Received: 30 December 2021 / Accepted: 16 June 2022 / Published online: 23 July 2022

Abstract
This research article presents the current challenges faced by our ecosystem due to depletion and insufficient fresh water bodies. In this current work, a novel holistic approach for the removal of toxic cadmium heavy metal ion from water using yttrium iron garnet is demonstrated. The impact of annealing temperature on the formation of garnet ferrite phase was investigated. The crystal structure analysis was investigated using X-ray diffraction (XRD) and further analyzed using Rietveld refinement technique. The surface morphology and functional groups were analyzed using high-resolution scanning emission microscopy (HR-SEM), Fourier transform infrared spectroscopy (FTIR), and Raman spectroscopy in detail. The magnetic property variation with respect to annealing temperatures was assessed from the data acquired from vibrating sample magnetometer (VSM) studies done at room temperature. X-ray photoelectron spectroscopy (XPS) chemical analysis technique was used to study the oxidation states of cations in the sample. To our knowledge, the utilization of yttrium iron garnet (YIG) as a magnetic adsorbent is extremely rare. So, in this article, we report the nature, important characteristics, and advantages of utilizing YIG nanoparticles for the eradication of cadmium for the treatment of water using atomic adsorption spectroscopy (AAS) technique. The experimental data was interpreted using adsorption isotherm modelling such as Langmuir and Freundlich isotherms.

Keywords YIG · Heavy metal · Adsorbent · Optimized temperature

1 Introduction

Fast industrialization and urbanization are the most significant reasons for the depletion and contamination of fresh water resources. Waste water from several industries such as leather tanning, battery manufacturing, metal coating, dye, and pigment production factories is discharged directly into water reservoirs without any treatment. They may contain organic or inorganic pollutants like hair, fertilizer, blood, heavy metals, synthetic dyes, pharmaceutical chemicals, and long-chained polymers. These non-biodegradable pollutants promote bioaccumulation inside living beings and cause major health issues to the environment [1]. In particular, heavy metal ions are cytotoxic, genotoxic, mobile, and soluble in nature. The World Health Organization (WHO) has elucidated various adverse effects in humans due to the presence of heavy metals such as lead (Pb), chromium (Cr), copper (Cu), nickel (Ni), manganese (Mn), silver (Ag), and cadmium (Cd). It has proposed maximum contaminant limit (MCL) for the use of heavy metals in water and found that excessive exposure to certain metal ions can inactivate enzymes, replace phosphate ions, oxidize biological molecules, and cause diffusion through cell membranes to deteriorate health completely [2]. It has also reported cadmium Cd(II) as the most life-threatening element among heavy metals. Official statistics reveal that the maximum limit of cadmium in drinking water specified as 0.005 mg/L is found to cause major destruction in human body even at less consumption [3]. For instance, Muibat et al. (2016) [4] reported that the impact of toxic heavy metals in living system has

✉ S. Pauline
paulinesusai@gmail.com

[1] Department of Physics, Loyola College, University of Madras, Chennai 600034, India

[2] SSN Research Centre, SSN College of Engineering, Kalavakkam 603110, Tamilnadu, India

[3] Department of Chemical Engineering, Indian Institute of Technology Madras, Chennai 600036, India

caused adenocarcinoma, dyspepsia, skin dermatitis, ulceration, hemorrhaging, and tissue gangrene, and also affects the kidney, liver, brain, genital system, and nervous system eventually leading to death. So, the scientific community constantly proposed several advanced techniques such as photocatalysis [5], solvent extraction [6], filtration processes [7], adsorption [8], and ion exchange [9] methods to combat this global issue. Among them, adsorption technique is the most significant method which allows easy operation, economical, and reliable abilities. Specifically, nanosized adsorbents are found play typical role in purifying water from unwanted pollutants for their promising features [10]. Harikishore et al. [11] also explain that a perfect adsorbent should possess (i) speedy adsorption, (ii) cost-efficiency, (iii) reusability, (iv) non-toxicity, and (v) effective dissociation. In recent times, magnetic nanoparticles have reached pinnacle in the field of research to solve numerous environmental problems. Nonetheless, magnetic nanoparticles are recognized as potential candidates for the promising adsorption technique [12]. An overview on the advancement of the functionalization of ferrite nanoparticles employed in the eradication of heavy metals from water effluent is presented below.

For example, magnesium ferrite nanospheres exhibited high adsorption capacity for the elimination of hazardous heavy metals when compared to other magnetic adsorbents such as Fe_3O_4, γ-Fe_2O_3, and α-Fe_2O_3 [13]. An inexpensive rapid and easy adsorption method was adopted for the removal of cadmium and lead ions using spinel ferrites MFe_2O_4 (M = Co, Ni, Cu, Zn). Of which copper ferrite exhibited higher adsorption capacity at about 157.7 mg/g to treat Cd^{2+} while cobalt ferrite adsorbs Pb^{2+} at an adsorption capacity of about 63.1 mg/g [14]. Recently, Y. Yu et al. [15] reported the superior adsorption and excellent dissociation property of yttrium-doped iron oxide adsorbent when compared to other magnetic adsorbents such as Fe_2O_3 cellulose composite, manganese spinel ferrites, Fe_3O_4 nanoparticles, and zirconium-based magnetic adsorbents. Furthermore, they suggest that the effective adsorption process is due to the presence of additional functional groups, more active sites, and bonding between Y–O-M and Fe–O-M linkages. Yttrium iron garnet ($Y_3Fe_5O_{12}$) from garnet family is a well-known rare earth ferrite which is widely used in microwave devices, multi-ferroics, permanent magnets, and also in radars [16]. Specifically, all sites in YIG are occupied with metal cations which make them more chemically stable and compatible than other spinel ferrite nanoparticles [17]. Saswat Kumar Pradhan et al. [18] emphasize that the addition of yttrium in alloys improves the workability as an adsorbent. Unfortunately, the use of garnet ferrite in adsorption technique is rarely explored and reported. Hence, with an inquisitive and novel approach in this study, yttrium iron garnet is taken as a magnetic adsorbent for the removal of hazardous cadmium metal ion. The effect of annealing temperature on the synthesis of YIG and on its property is also reported.

2 Experimental

In sol–gel method, the raw materials iron nitrate nonahydrate ($Fe(NO_3)_3{\cdot}9H_2O$) and yttrium nitrate hexahydrate ($Y(NO_3)_3{\cdot}6H_2O$), purchased from Sigma-Aldrich having 99.99% purity are used as starting materials. The metal nitrates with 3 mol of yttrium nitrate, 5 mol of iron nitrate, and citric acid which act as the chelating agent were dissolved in the ratio of 1:1[MN:CA] in 160 mL of water. The aqueous solution was stirred using a digital display heating magnetic stirrer at a rotation speed of 310 RPM for 1 h and heat treated for 80 °C with continued stirring until the formation of gel. Then the temperature was increased up to 250 °C led to the ignition of the gel. The dried gels burnt in an auto-combustion manner until the gels were completely burnt out to form a loose powder. The loose dried powder was further ground manually for 2 to 3 h and finally, annealed at various temperatures 650 °C, 850 °C, 1050 °C, and 1250 °C for 4 h for the formation of YIG.

The chemical reaction of these mixtures forming YIG is as follows:

$$3Y(NO_3)_3 \cdot 6H_2O + 5Fe\left(NO_3\right)_3 \cdot 9H_2O + 8C_6H_8O_7 \cdot H_2O \rightarrow 3YC_6H_5O_7 + 5FeC_6H_5O_7 + 24HNO_3 + 71H_2O \quad (1)$$

$$3YC_6H_5O_7 + 5FeC_6H_5O_7 + O_2 \rightarrow Y_3Fe_5O_{12} + 20H_2O + 48CO_2 \quad (2)$$

For the adsorption process, the as-prepared adsorbent was added to cadmium-polluted water and was continuously agitated using sophisticated copper stirrer equipment for various time intervals such as 6, 12, 18, and 24 h at room temperature. The aliquot of the sample was collected using a ready to use nylon filter syringe with pore size 0.22 µm and diameter 25 mm and then analyzed for atomic adsorption spectroscopy (AAS) experiment.

2.1 Characterization

The identification of phase and structure of the prepared samples at different temperatures were investigated using X-ray diffractometer (Bruker D8 advance) operated at 40 kV and at 30 mA with CuKα radiation ($\lambda = 1.5406$ Å). FEI Quanta FEG 200—high-resolution scanning electron microscope was used to examine the surface morphology of the sample. Fourier transform infrared (FTIR) spectra were recorded using a Perkin-Elmer spectrometer, model (2000), which ranges from 400 to 4000 cm^{-1} and Raman spectra was

also analyzed using LASER Raman spectroscopy analysis. The magnetic property of the samples was analyzed using vibrating sample magnetometer (VSM) Lakeshore model (7407) at room temperature. The prepared product was characterized using thermogravimetric (TG) and differential thermal analysis (DTA) (SDT Q600, TA, USA) at a heating rate of 10 °C/min in static air. The XPS spectrum was taken using X-ray photoelectron spectroscopy (XPS, PHI-5000). The adsorption capacity of the sample was studied using atomic absorption spectrometer (AAS).

3 Results and Discussion

3.1 XRD Analysis of YIG Nanoparticles

The XRD pattern clearly depicts the phase formation with different annealing temperatures. Figure 1a clearly represents the amorphous nature of the dried sample and its persistent amorphous nature till temperature 550 °C. As shown in Fig. 1b at 650 °C, a diffraction peak at $2\theta = 33.12°$ is obtained, which is indicative of secondary $YFeO_3$ phase. Further increment in temperature provides sufficient energy to convert $YFeO_3$ phase into $Y_3Fe_5O_{12}$ phase. So, beyond 1000 °C, most intense well-defined signature peak gets shifted to $2\theta = 32.2°$ which projects the high crystalline nature of YIG phase [19]. The gradual increase in garnet phase and decreasing trend of yttrium ortho ferrite phases is clearly depicted in the figure. Interestingly, all the peaks exactly matched the standard JCPDS data (75–1852).

$$[\blacklozenge - YFeO_3, \bullet - Y_2O_3 \spadesuit - Fe_2O_3 \heartsuit - Y_3Fe_5O_{12}]$$

The average crystallite size was calculated using the Scherrer formula,

$$D = \frac{K\lambda}{\beta \cos\theta} \tag{3}$$

where λ is the wavelength of incident radiation, β is the full width at half maximum (FWHM), K varies with hkl & crystallite shape is equal to 0.89 and θ is the Bragg's angle [20]. The crystallite size of samples prepared at different annealing temperatures 650 °C, 850 °C, 1050 °C, and 1250 °C was calculated and tabulated in Table 1.

Table 1 Parameters calculated from XRD analysis

Sample	D (nm)
Y-650 °C	39.75
Y- 850 °C	63.94
Y-1050 °C	88.69
Y-1250 °C	96.52

Combustion is a process for producing highly crystalline ceramic powders that involves a redox combination of precursor salts (oxidants) and a fuel (reducing agent). According to propellant chemistry, the fuel-to-oxidant ratio in combustion reactions is set so that the fuel's net reducing valency equals the oxidant's net oxidizing valency [21]. The type of fuel, the fuel-to-oxidizer ratio, and the ignition temperature have an impact on the combustion synthesis reaction. The exothermic temperature of the redox reaction ranges from 1000 to 1500 °C depending on the material [22]. In this work, the oxidants are the metal nitrates and the fuel is citric acid. The combustion temperature of YIG is obtained at 650 °C where the amorphous nature is transformed to crystalline nature. However, the combusted product was further ignited to 1250 °C to obtain pure YIG nanoparticles.

The crystallographic structure of the prepared YIG from XRD pattern was analyzed by Rietveld refinement using FULLPROF software and is depicted in Fig. 1. The diffraction peaks were fitted using pseudo-voigt function and 6-coefficients polynomials function as background (Fig. 2). The garnet samples are found to exhibit cubic structure with space group O_h^{10}—Ia3d. The reliability R-factors: expected R_{exp}, Bragg R_{Bragg}, profile R_p, and weighted profile R_{wp} less than 10% are usually used to determine the Rietveld fitting quality. From Table 2, it is inferred that the R-factors are less than 10% which is indicative of good fit [23, 24].

3.2 Morphological Analysis of YIG Nanoparticles by HR-SEM

The typical SEM micrographs shown in Fig. 3 indicate the variation in morphology and shape of ferrite nanoparticles with respect to annealing temperature. At 650 °C, agglomerated spherical-like structure was obtained due to incompletion of reaction, whereas the sample annealed at 850 °C develops indefinite boundaries in the sample [19]. At higher temperatures, the agglomeration reduces drastically and begins to change its shape, by forming uniform definite boundaries. A closely packed honey-comb like shape is obtained at 1250 °C. This tendency for change in

Table 2 Reliability factors calculated from Rietveld refinement method

Reliability factors	YIG (1250 °C)	YIG (1050 °C)
Rb (%)	4.381641	4.032012
Rwp (%)	7.572881	6.622285
Rexp (%)	3.224285	3.174692
χ^2(%)	2.35	2.085

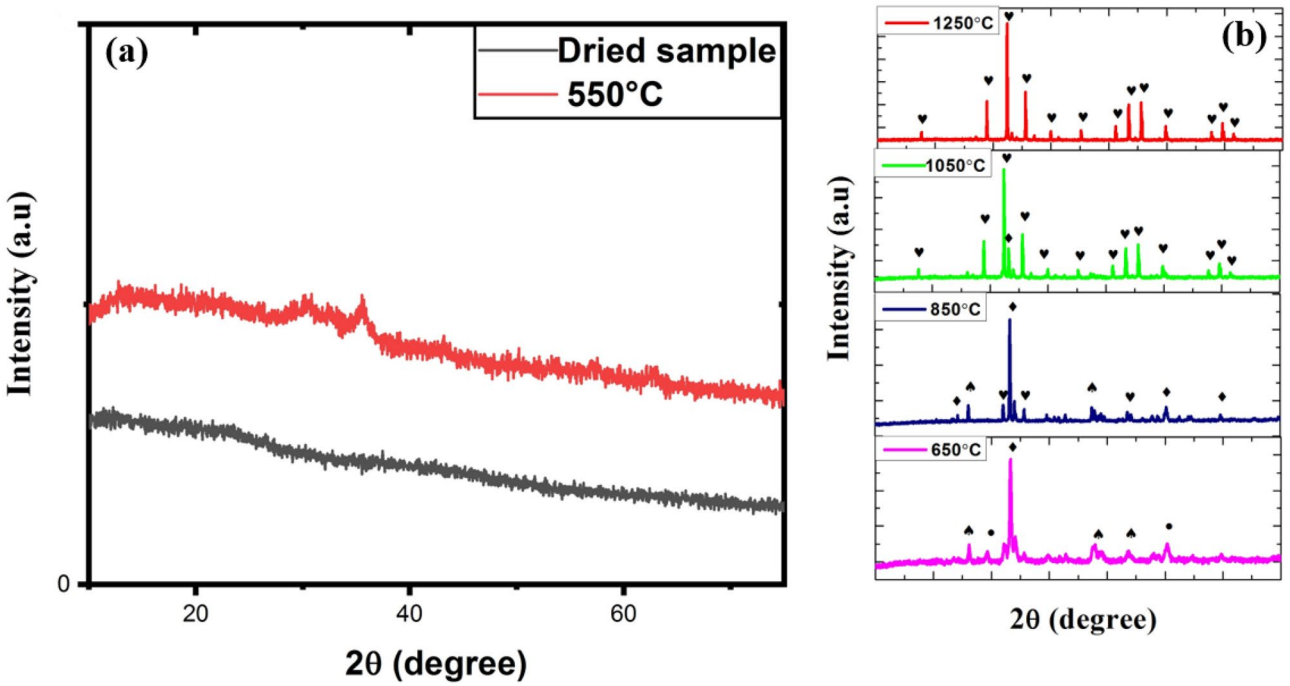

Fig. 1 **a** XRD patterns of dried sample and sample heated at 550 °C; **b** XRD patterns of YIG nanoparticles annealed at 1250 °C, 1050 °C, 850 °C, and 650 °C

size and shape could also be related due to the breaking and welding of particles [25].

3.3 The Vibrational Spectroscopic Analysis of YIG Nanoparticles

FTIR spectra of YIG nanoparticles are shown in Fig. 4. At temperatures beyond 1000 °C, the spectrum exhibited three bands at 649 cm^{-1}, 604 cm^{-1}, and 550 cm^{-1} which is attributed to the asymmetric stretching modes of tetrahedron and confirms the presence of garnet ferrite nanoparticles [26]. Spectroscopic bands at 1628 cm^{-1} and 3414 cm^{-1} correspond to carboxyl group and O–H group respectively. At 650 °C, the band prominent at 425 cm^{-1} is indicative of yttrium ortho ferrite $YFeO_3$ phase begins to diminish with increasing temperatures and thereby, represents the progression of YIG phase with increase in temperature [27].

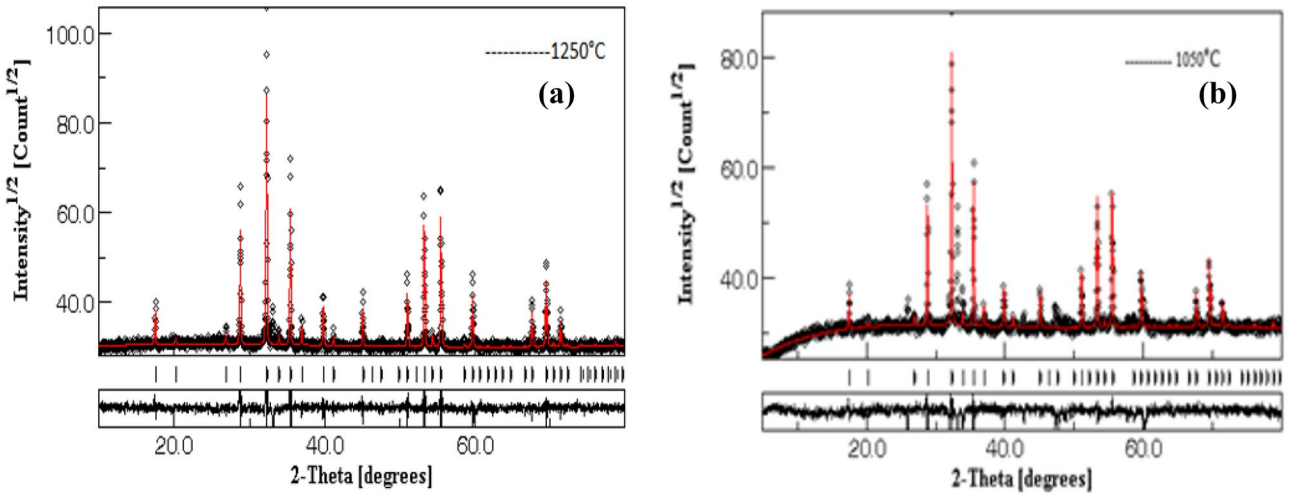

Fig. 2 **a–b** Rietveld refinement of YIG nanoparticles annealed at 1250 °C and 1050 °C

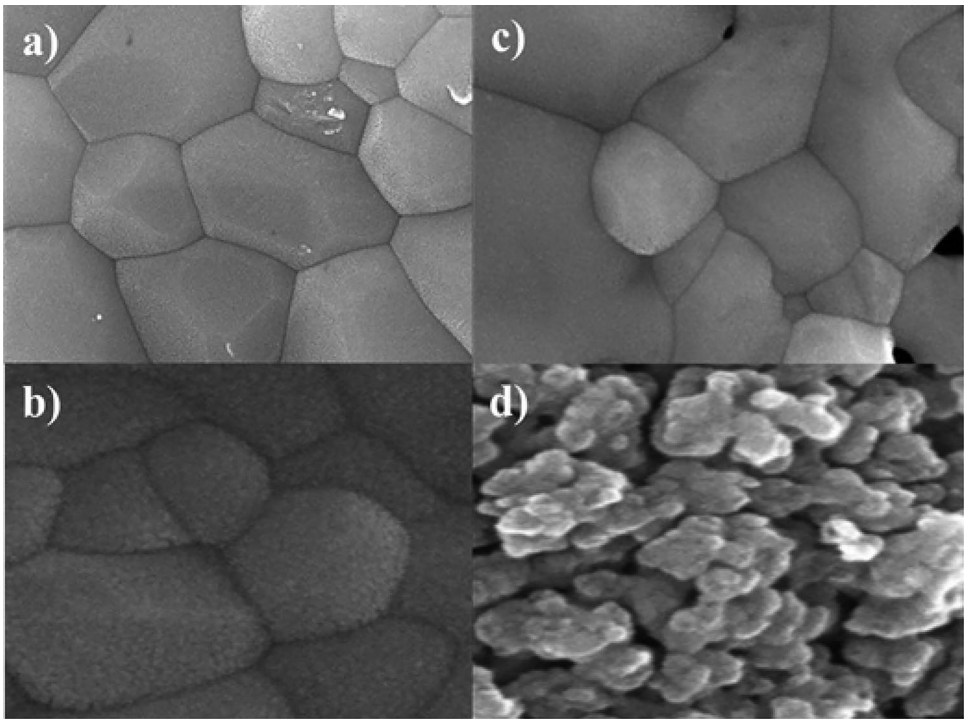

Fig. 3 HR-SEM images of YIG nanoparticles prepared at different annealing temperatures such as **a** 1250 °C, **b** 1050 °C, **c** 850 °C, and (**d**) 650 °C

3.4 Raman Spectra Analysis of YIG Nanoparticles

The Raman spectrum of YIG is shown in Fig. 5. The samples annealed at 1050 °C and 1250 °C show a major peak at 270 cm^{-1} which confirms the presence of garnet phases. Initially at 650 °C, the peaks obtained at 290 cm^{-1} and 220 cm^{-1}, and 180 cm^{-1} and 400 cm^{-1} correspond to Fe_2O_3 and Y_2O_3 molecules respectively. Beyond 1000 °C, the remnant Fe_2O_3 reacts to form YIG by shifting the band from 292 to 270 cm^{-1}. However, the peaks observed at 160 cm^{-1}, 220 cm^{-1}, 260 cm^{-1}, 340 cm^{-1}, and 370 cm^{-1} are due to the vibrations of yttrium ions in the YIG sample [28, 29]. As reported earlier, peaks that arise below 300 cm^{-1} are due to the various motions of RO8 (dodecahedral), FeO_6 (octahedral), and also due to the liberation modes of FeO_4 (tetrahedral) [30].

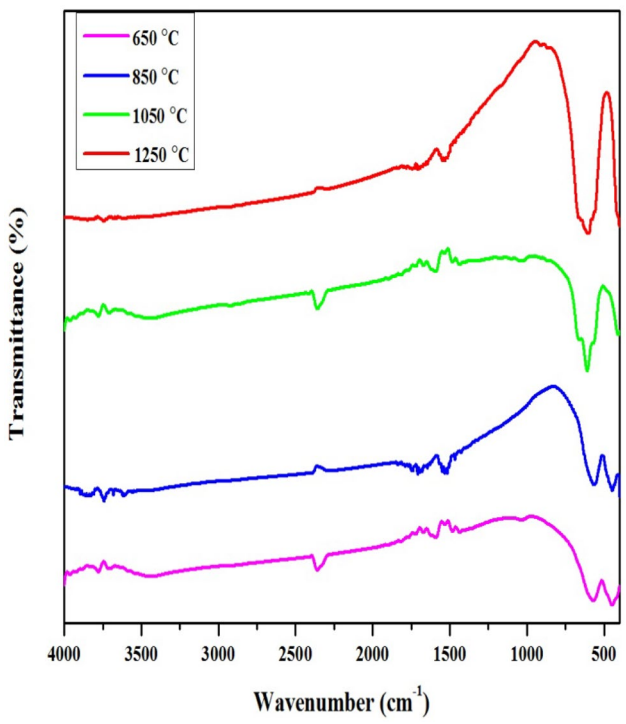

Fig. 4 FTIR spectra of YIG nanoparticles prepared at different temperatures such as 650 °C, 850 °C, 1050 °C, and 1250 °C

3.5 Magnetic Properties of YIG Nanoparticles

Magnetic properties were evaluated using VSM at room temperature. Well-defined sigmoid shape loops and its variation with temperatures are shown in Fig. 6. The saturation magnetization M_s values are found to increase and coercivity (Hc) values are found to decrease with increasing temperatures. This is because both these parameters are reciprocal to each other ($H_c \alpha 1/M_s$) as mentioned in [31] and is also depicted in Fig. 7. Additionally, the transition from single domain to multidomain moments is responsible for the variation in saturation (M_s), remanance (M_r), and coercivity (H_c) values in the samples [32].

Magnetic properties of YIG samples are shown in Table 3. Consequently, these estimated values are found to be comparable with Emami et al. [33]. These saturation magnetization values M_s of few hundred Oersteds of coercivity H_c indicate strong magnetism and soft nature of garnet

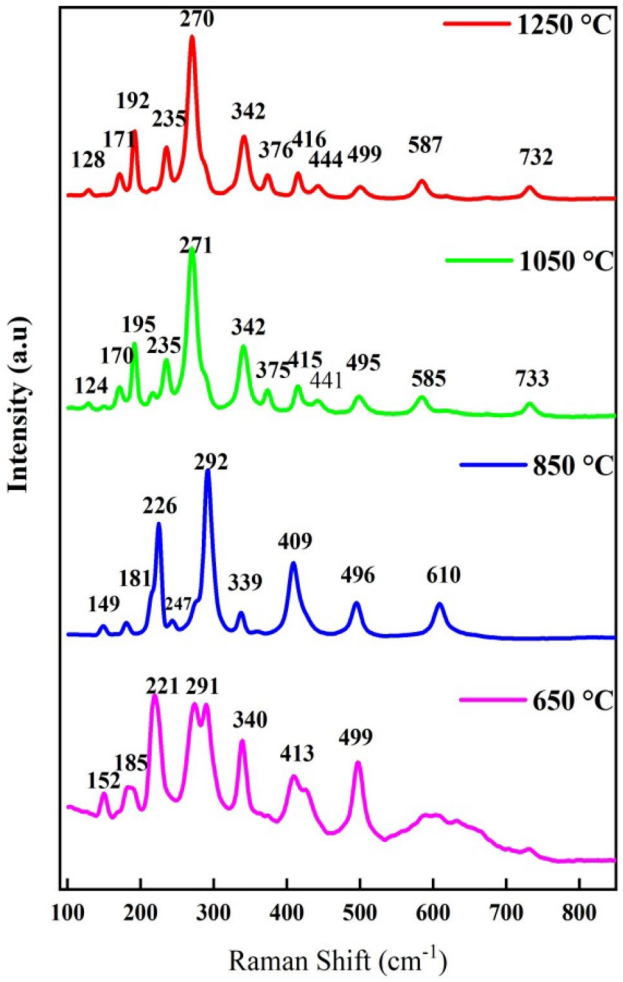

Fig. 5 Raman spectra of YIG nanoparticles at prepared 1250 °C, 1050 °C, 850 °C, and 650 °C annealing temperatures

ferrites which are the main attributes for many applications. These values are found to be dependant on the intrinsic (composition, synthesis method) and extrinsic properties (morphology, porosity) of garnet ferrites [25].

3.6 TG–DTA Thermal Analysis of YIG Nanoparticles

Figure 8a, b represent the thermal analysis of pre-combusted and combusted product respectively. Initially three peaks were observed in the pre-combusted sample in which the

Table 3 Parameters calculated from VSM analysis at room temperature

Parameters	*D* (nm)	Ms (emu/g)	Hc (Oe)
Y-650 °C	39.75	11.39	252.13
Y-850 °C	63.94	14.85	174.85
Y-1050 °C	88.69	18.72	133.01
Y-1250 °C	96.52	22.01	113.96

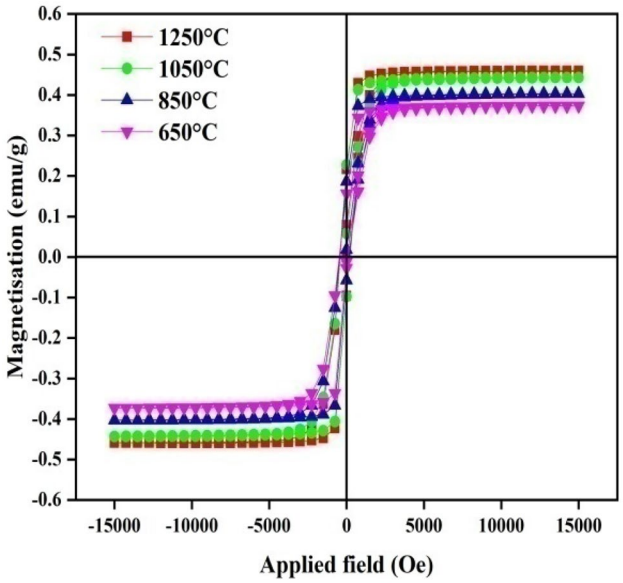

Fig. 6 M-H loops of YIG nanoparticles annealed different temperatures such as 650 °C, 850 °C, 1050 °C, and 1250 °C

removal of residual water in the dried sample is obtained in the region of 150–170 °C. The reaction of metal nitrate and citric acid produced a sharp exothermic peak at 170 °C with a weight loss of 73%. Two exothermic peaks in the 240–355 °C range were eventually observed, corresponding to the decomposition of remaining citric acid and the oxidation of residual carbon formed during the rapid combustion reaction. It is understood that the combination of nitrate and citrate gels resulted in a self-propagating combustion reaction at temperatures ranging from 120 to 180 °C. Due to the rapid release of gases such as NO and CO_2 [34], this quickly burns out into an aggregate loose powder that is porous [35]. The exothermic peak also suggested that this was due to the decomposition involved oxidation of residual carbon that occurred during the combustion process.

There was no weight loss when the temperature was higher than roughly 370 °C, indicating that the processes had come to a halt. At around 645 °C, a minor exothermic peak was discovered, which corresponded to the crystallization of the amorphous phase which in turn confirmed the combustion process. Hence, the crystallization temperature 645 °C deduced from the TG–DTA coincides well with the XRD report [36].

3.7 XPS Analysis of YIG Nanoparticles

XPS technique was employed to determine the oxidation states of cations due to its high sensitivity towards surface structure of pure YIG. The samples were analyzed by XPS to study the surface components and the valence of elements present in the sample [37]. The presence of all basic

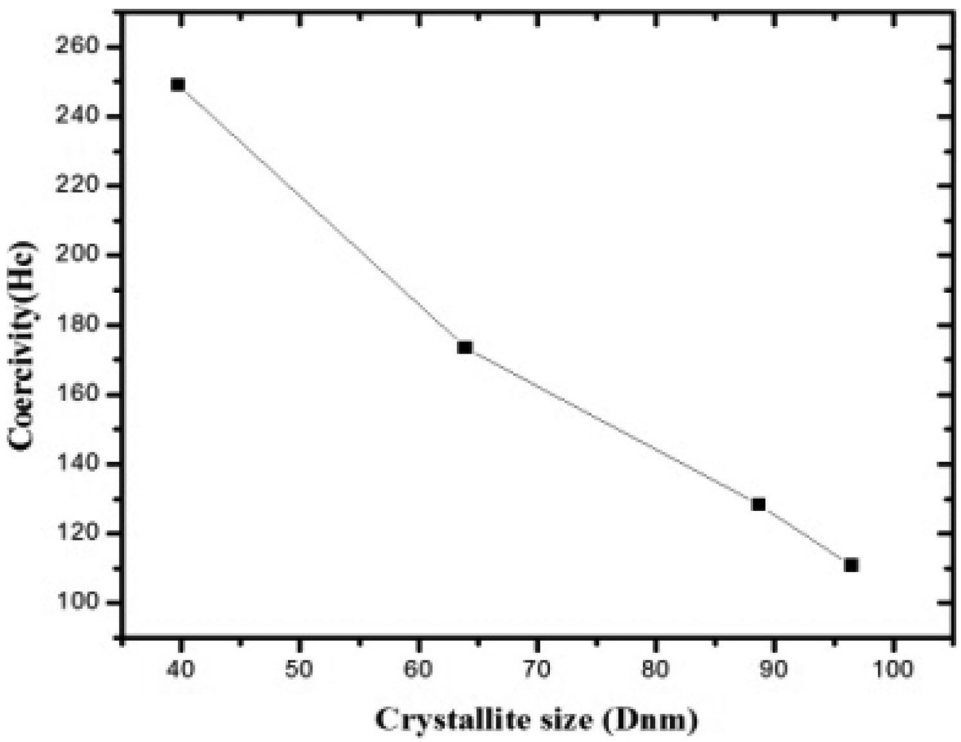

Fig. 7 Correlation between coercivity (Hc) and crystallite size (Dnm) of YIG nanoparticles

elements, namely Y, Fe, and O is clearly visible in the survey spectra.

Based on the Lorentzian-Gaussian fitting, the yttrium characteristic peak is divided into two component peaks with binding energies of 157.3 and 159.2 eV corresponding to $Y_{3d5/2}$ and $Y_{3d3/2}$ states respectively [19]. Fe-2p state splits into two components such as $2p_{1/2}$ and $2p_{3/2}$ and is shown in Fig. 9. The oxidation state of Fe which consists of Fe^{2+} and Fe^{3+} usually represented as an asymmetric broad peak is centered at 710.2 eV. $Fe_{2p3/2}$ and $Fe_{2p1/2}$ states can be subdivided into sub-bands such as $Fe^{3+}{}_{2p3/2}$, $Fe^{2+}{}_{2p3/2}$, $Fe^{3+}{}_{2p1/2}$, and $Fe^{2+}{}_{2p1/2}$ [38]. The existence of Fe^{2+} ions in $Y_3Fe_5O_{12}$ ceramics is due to the low oxygen conditions at high temperature sintering process [39]. Figure also represents the analysis of oxygen vacancies in YIG ferrite. It exhibits the sum of two separated peaks represented as O 1 s. From which the peak present at O [1] 529.4 eV indicates the oxygen ions in the lattice and O [2] peak at 531.1 eV is indicative of oxygen vacancies [40]. Therefore, the XPS studies confirm the existence of Y, Fe, and O in YIG ferrite.

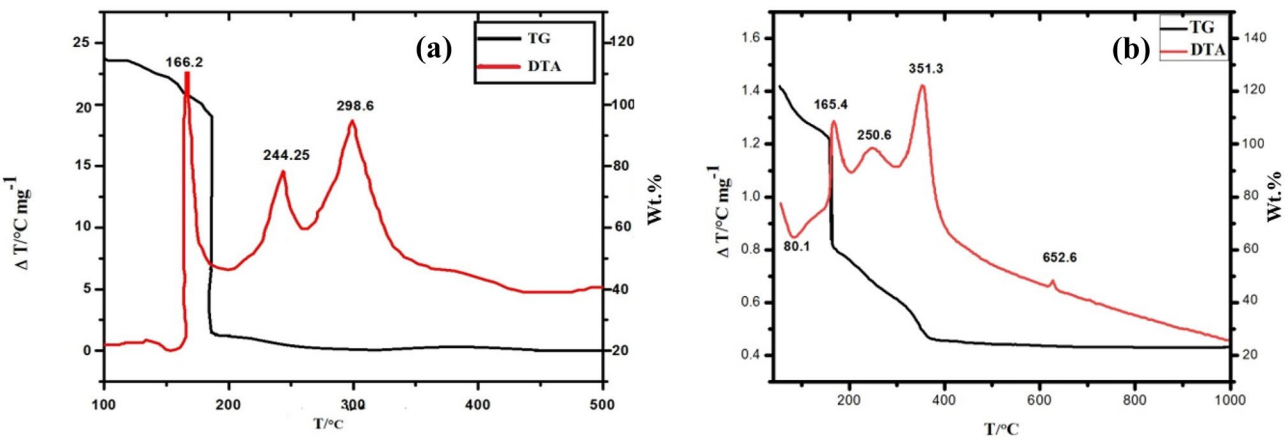

Fig. 8 TG–DTA thermal analysis of **a** pre-combusted and **b** combusted product of YIG nanoparticles

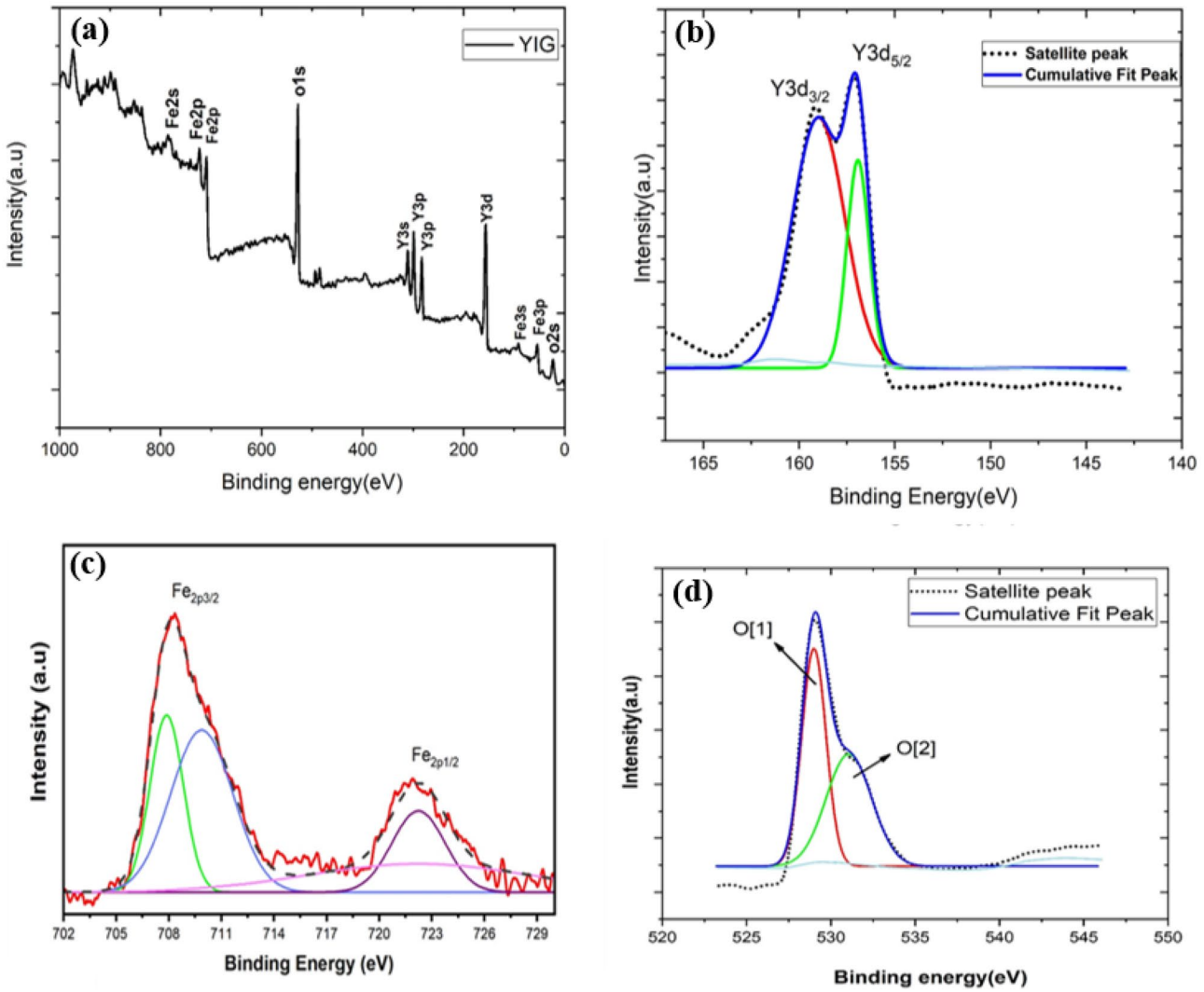

Fig. 9 **a** XPS full survey spectrum. **b** Y 3d. **c** Fe 2p. **d** O 1 s spectra of YIG nanoparticles

3.8 Adsorption Capacity Measurements and Adsorption Mechanism

For the adsorption process, 20 ppm of cadmium was dissolved in water to form a homogenous solution. The chemical condition of the medium was maintained at pH ~ 7. YIG was introduced as an adsorbent and was agitated continuously for 6 h, 12 h, 18 h, and 24 h. The amount of adsorption and their removal efficiency was calculated using Eqs. (4) and (5):

$$q_e = \frac{V(C0 - Ce)}{W} \tag{4}$$

$$e = \frac{C0 - Cf}{C0} \times 100\% \tag{5}$$

where q_e is the amount of adsorbed metal (mg/g), e is the removal efficiency, C_0 is the concentration of initial adsorbate (mg/L), C_e is adsorbate concentration at equilibrium (mg/L), C_f is the final adsorbate concentration, V is the volume of the adsorbate (L), and W is the mass of the adsorbent (mg). The removal efficiency of garnet ferrite was found to increase from 17.80 to 41.13% with increasing time intervals from 6 to 24 h and is depicted in Fig. 11a. This adsorption mechanism is mainly attributed due to the formation of complex of hydroxyl and carboxyl functional groups and ion exchange mechanism. The complex formation of YIG and cd (oxyanion) is as follows:

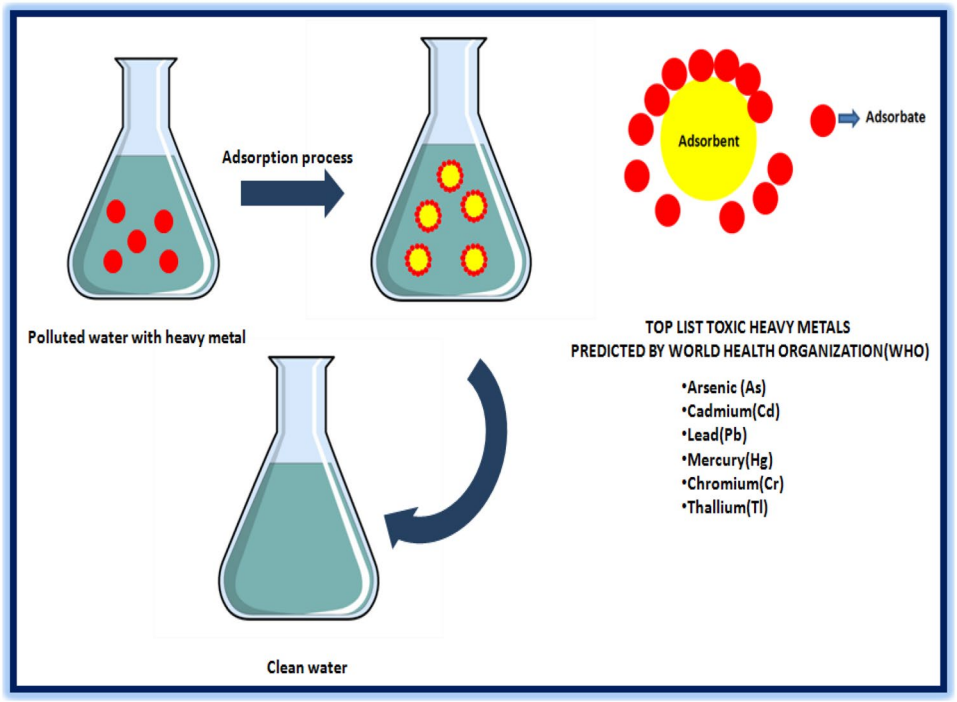

Fig. 10 Adsorption mechanism

$$2ROH^{-}_{(s)} + M^{2+}{}_{(aq)} \Leftrightarrow [(RO^{-})_2M^{2+}]_{(s)} + 2H^{+} \quad (6)$$

$$2RCOO^{-}_{s} + M^{2+}{}_{(aq)} \Leftrightarrow [(RCOO^{-})_2M^{2+}]_{(s)} \quad (7)$$

where R indicates the surface of YIG and M indicates cadmium ions.

This is also attributed to the intrinsic factors which correspond to the selectivity of adsorbent and extrinsic factors like pH, temperature, NP's loading, and concentration of heavy metals [14]. The adsorption mechanism is depicted in Fig. 10. As post-treatment of the absorbent has always been the topic of concern for industrial application, YIG (1250 °C) was found to be regenerated thrice successfully and is represented in Fig. 11b. For this regeneration experiment, the utilized adsorbent was separated using an external magnetic field, then treated with a 0.5-M NaOH solution under agitation for 6 h, washed, dried, and used for the next cycle of the adsorption processes. The experiment demonstrates the regeneration efficiency after separation. Similarly, the consistent decline during regeneration experiment was also encountered [41] which will be investigated in future.

The adsorption mechanism can be explained using sorption isotherm modelling which provides a deeper understanding of how metal ions interact with the active spots on the sorbent surface. The isotherm data are usually fitted using Langmuir and Freundlich isotherms. In which Langmuir isotherm assumes that sorption is due to monolayer possessing independent equivalent active sites, whereas Freundlich isotherm assumes that sorption is due to multilayer active sites. Very good fitting was observed using Freundlich isotherm in which the correlation coefficient R^2 is almost equal to one and is represented in Fig. 11c–d. Hence, the high affinity of YIG towards Cd metal ions developed multi-layered complexes of surface functional groups for the remediation process. These available active sites shortened the equilibrium level by increasing the driving force and thereby hastened the reaction. Besides, the sample's resistivity, surface functional groups, thermal stability, and magnetic properties are also responsible for this adsorption effect.

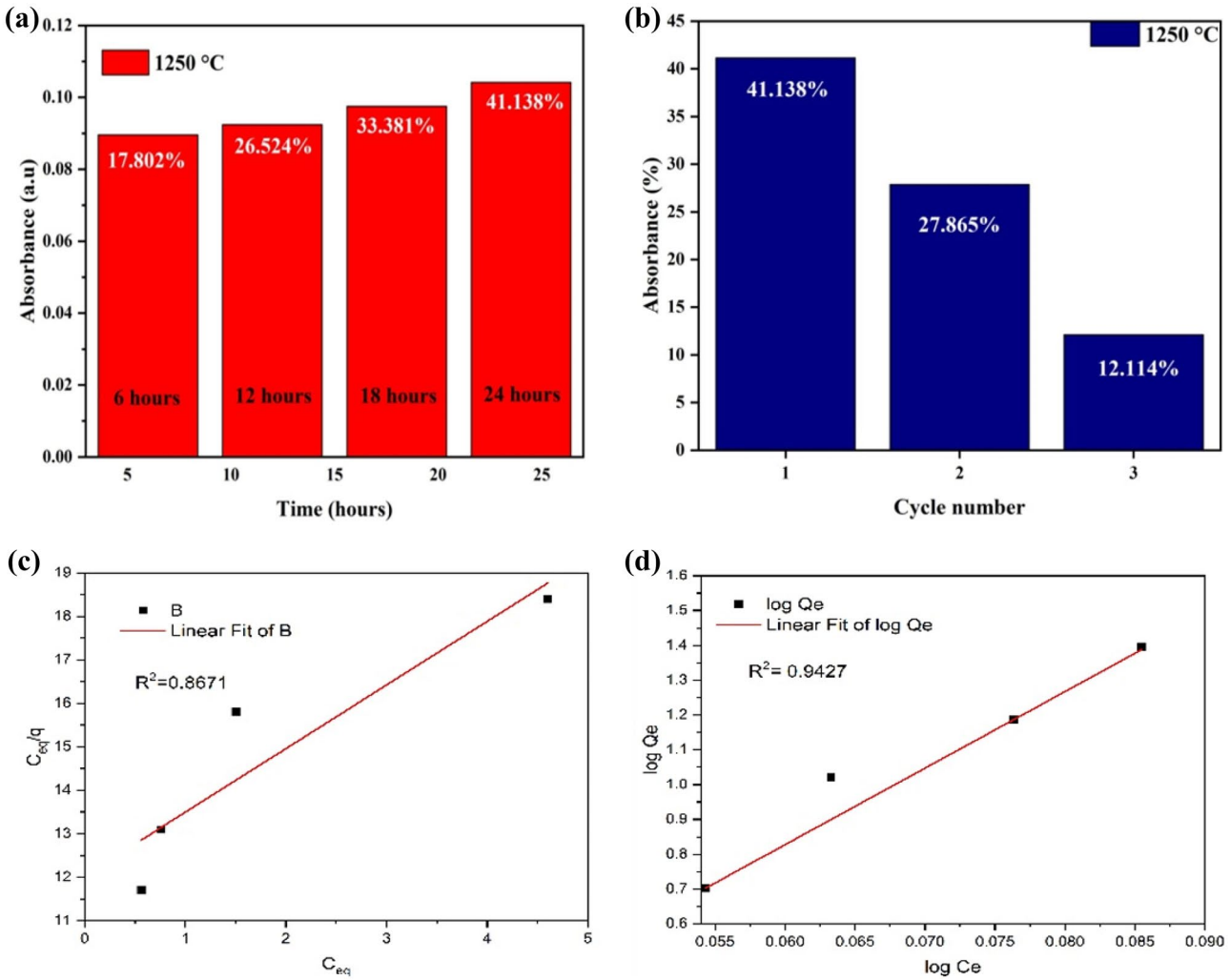

Fig. 11 **a** The adsorption capacity of toxic Cd by YIG at various time intervals 6, 12, 18, and 24 h. **b** Regenerated experiment of YIG during cadmium remediation process. **c–d** Langmuir and Freundlich isotherm models of YIG nanoparticles

4 Conclusion

YIG garnet samples were used to eradicate cadmium which is listed as one of the most toxic element by the World Health Organization (WHO), through adsorption technique. The XRD results reveal the existence of garnet phase with significant peak [420] that is successfully developed only at high temperatures beyond 1000 °C. Rietveld refinement of XRD pattern confirms the cubic structure of the sample and produced a good fit. At high temperature, well-defined honey comb-like shape was clearly obtained from HR-SEM without any agglomeration. The vibrational spectra from FTIR and Raman analysis bring out the different functional groups and their bonding. TG–DTA thermal analysis and XPS study of YIG were in good correlation with the XRD report. The magnetic properties were found to depend on the preparation conditions and heat treatment. Most importantly, the contribution of YIG magnetic nanoadsorbent provides a viable solution in treating the alarming water pollution problem by industries. This adsorbent is very much advantageous than other adsorbents due to its easy separable and regeneration characteristics. The YIG sample shows a maximum adsorption capacity of 41.138% at 24 h and was regenerated three times portraying it as a potential adsorbent for the eradication of toxic cadmium metal ions from water. And also, the equilibrium adsorption of YIG on Cd^{2+} was described as heterogenous layer of sorption process using Freundlich isotherm model. In future, this adsorbent can be composited with carbon-based materials for spontaneous adsorption to treat heavy metal polluted water with promising recyclability or may also be used as a magnetic separator as an alternative for other ferrites.

References

1. Anh Thi Le: Swee-Yong Pung. Srimala Sreekantan, Atsunori Matsuda, Mechanisms of removal of heavy metal ions by ZnO particles, Heliyon **5**(4), e01440 (2019)
2. Lal, S., Singhal, A., Kumari, P.: Exploring carbonaceous nanomaterials for arsenic and chromium removal from wastewater. Journal of Water Process Engineering **36**, 101276 (2020)
3. Nasehi, P., Mahmoudi, B., Abbaspour, S.F., Moghaddam, M.S: Cadmium adsorption using novel $MnFe_2O_4$-TiO_2-UIO-66 magnetic nanoparticles and condition optimization using a response surface methodology, RSC Advances **9**(350), 20087–20099 (2019)
4. Muibat Omotola Fashola: Veronica Mpode Ngole - Jeme, Olubukola Oluranti Babalola, Heavy metal pollution from gold mines: environmental effects and bacterial strategies for resistance. Int. J. Environ. Res. Public Health **13**(11), 1047 (2016)
5. Vinosel, V.M., Anand, S., Janifer, M.A., Pauline, S., Dhanavel, S., Praveena, P., Stephen, A.: Enhanced photocatalytic activity of Fe_3O_4/SnO_2 magnetic nanocomposite for the degradation of organic dye. J. Mater. Sci. Mater. Electron. **30**(10), 9663–9677 (2019)
6. Borowiak-Resterna, A., Cierpiszewski, R., Prochaska, K.: Kinetic and equilibrium studies of the removal of cadmium ions from acidic chloride solutions by hydrophobic pyridine carboxamide extractants. J. Hazard. Mater. **179**(1–3), 828–833 (2010)
7. Raghavendra, S. Hebbar, A.M., Isloor, K. Ananda, A.F.: Ismail, Fabrication of antifouling, antimicrobial, well dispersed polydopamine functionalized halloysite nanotube-polyetherimide mixed matrix membranes for the heavy metal removal application, J. Mater. Chem. A. **4** 764–774 (2016)
8. Abbas, A., Al-Amer, A.M., Laoui, T., Al-Marri, M.J., Nasser, M.S., Khraisheh, M., Atieh, M.A: Heavy metal removal from aqueous solution by advanced carbon nanotubes: critical review of adsorption applications. Separation and Purification Technology. **157**, 141–161 (2016)
9. Zewail, T.M., Yousef, N.S.: Kinetic study of heavy metal ions removal by ion exchange in batch conical air spouted bed. Alex. Eng. J. **54**(1), 83–90 (2015)
10. Wadhawan, S., Jain, A., Nayyar, J., Mehta, S.K.: Role of nanomaterials as adsorbents in heavy metal ion removal from waste water: a review. J. Water Proc. Eng. **33**, 101038
11. Harikishore, D., Reddy, K., Yun, Y.S.: Spinel ferrite magnetic adsorbents: alternative future materials for water purification, Coordination Chem Rev **315**, 90–111 (2016)
12. Inbaraj, D.J., Chandran, B., Mangalaraj, C.: Bagavath Chandran, Chitra Mangalaraj, Synthesis of $CoFe_2O_4$ and $CoFe_2O_4$/g-C_3N_4 nanocomposite via honey mediated sol-gel auto combustion method and hydrothermal method with enhanced photocatalytic and efficient Pb^{2+} adsorption property. Materials Research Express **6**(5),(2019)
13. Can, Wu., Jingwei, Tu., Tian, C., Geng, J., Lin, Z., Dang, Z.: Defective magnesium ferrite nano-platelets for the adsorption of As (V): the role of surface hydroxyl groups. Environ. Pollut. **235**, 11–19 (2018)
14. Al Yaqoob, K.M., Bououdina, M.S., Akhter, B., Al Najar, J., Vijaya, J.: Selectivity and efficient Pb and Cd ions removal by magnetic MFe_2O_4 (M= Co, Ni, Cu and Zn) nanoparticles. Mater. Chem. Phys. 232, 254–264 (2019)
15. Yu, Y., Yu, L., Shih, K., Paul Chen, J.: Yttrium-doped iron oxide magnetic adsorbent for enhancement in arsenic removal and ease in separation after applications. J. Colloid Interface Sci. **521**, 252–260 (2018)
16. Asisi Janifer, M.S Anand, S., Maria Vinosel, V., Pauline S.: Investigation of rare earth garnet and its physical properties synthesized by facile sol-gel method. Mater. Today Proc. **8**, 337–345 (2019)
17. Akhtar, M.N., Khan, M.A., Mukhtar Ahmad, G,. Murtaza, R.R., Shaukat, S.F., Asif, M.H.: $Y_3Fe_5O_{12}$ nanoparticulate garnet ferrites: comprehensive study on the synthesis and characterization fabricated by various routes. J. Magn. Magn. Mater. **368**, 393–400 (2014)
18. Pradhan, S.K., Panwar, J., Gupta, S.: Jitendra Panwar, and Suresh Gupta. Enhanced heavy metal removal using silver-yttrium oxide nanocomposites as novel adsorbent system, Journal of environmental chemical engineering **5**(6), 5801–5814 (2017)
19. Liu, J., Yu, P., Jin, Q., Zhang, C., Zhang, M.: Harris VG, Microwave-accelerated rapid synthesis of high-quality yttrium iron garnet nano powders with improved magnetic properties. Mater. Res. Lett. **2**(6), 36–40 (2018)
20. Anand, S., Amaliya, A.P., Asisi Janifer, M., Pauline, S.: Structural, morphological and dielectric studies of zirconium substituted $CoFe_2O_4$ nanoparticles. Mode. Elect. Mater. **3**(4), 168–173 (2017)
21. Lakshmi, V.: Vijaya. Ranjit Bauri, Soumalya Paul, Effect of fuel type on microstructure and electrical property of combustion synthesized nanocrystalline scandia stabilized zirconia, Materials chemistry and physics **126**(3), 741–746 (2011)
22. Kaliyamoorthy, V., Babu, D.R., Saminathan, M.: Impact of ignition temperature on particle size and magnetic properties of $CoFe_2O_4$ nanoparticles prepared by self-propagated MILD combustion technique. J. Magn. Magn. Mater. **418**, 280–288 (2016)
23. Anand, S., Pauline, S., Vinosel, V.M., Janifer, M.A.: Structural Rietveld refinement and vibrational study of M-type $BaFe_{12}O_{19}$ nanoparticles. Mater. Today Proc. **8**, 476–483 (2019)
24. Aparnadevi, N., Saravana Kumar, K., Manikandan, M., Paul Joseph, D., Venkateswaran, C.: Room temperature dual ferroic behaviour of ball mill synthesized $NdFeO_3$ orthoferrite. J. Appl. Phys. **120**(3), 034101 (2016)
25. Akhtar, M. N., Khan, M.A., Ahmad, M., Murtaza, G., Raza, R., Shaukat, S.F., Asif, M.F.: $Y_3Fe_5O_{12}$ nanoparticulate garnet ferrites: comprehensive study on the synthesis and characterization fabricated by various routes, Journal of magnetism and magnetic materials **368**, 393–400 (2014)
26. Niyaifar, M., Mohammadpour, H., Dorafshani, M., Hasanpour, A.: Size dependence of non-magnetic thickness in YIG nanoparticles. J. Magn. Magn. Mater. **409**, 104–110 (2016)
27. Modi, K.B., Dolia, S.N., Sharma, P.U.: Effect of mechanical milling induced strain and particle size reduction on some physical properties of polycrystalline yttrium iron garnet". Indian J. Phys. **89**(5), 425–436 (2015)
28. Nasir, N., Yahya, N., Kashif, M., Daud, H.: Majid Niaz Akhtar, Hasnah Mohd Zaid, Afza Shafie, Lee Chaw Teng, Observation of a cubical-like microstructure of strontium iron garnet and yttrium iron garnet prepared via sol–gel technique. J. Nanosci. Nanotechnol. **11**(3), 2551–2554 (2011)
29. Fernandez-Garcia, L.: Marta Suárez, and José Luis Menendez, Synthesis of mono and multidomain YIG particles by chemical coprecipitation or ceramic procedure. J. Alloy. Compd. **495**(1), 196–199 (2010)
30. Sharma, V.: and Bijoy Kumar Kuanr, Magnetic and crystallographic properties of rare-earth substituted yttrium-iron garnet. J. Alloy. Compd. **748**, 591–600 (2018)
31. Sonia, M.M.L., Anand, S., Vinosel, V. M., Janifer, M. A., Pauline, S., Manikandan, A.: Effect of lattice strain on structure, morphology and magneto-dielectric properties of spinel $NiGd_xFe_{2-x}O_4$ ferrite nano-crystallites synthesized by sol-gel route. J. Magn. Magn. Mater. **466**, 238–251 (2018)
32. Sonia, M., Anand, S., Vinosel, V. M., Asisi Janifer, M., Pauline, S.: Effect of lattice strain on structural, magnetic and dielectric properties of sol-gel synthesized nanocrystalline Ce^{3+} substituted nickel ferrite. J. Mater. Sci. Mater. Electron. **29**, 15006–15021
33. Emami, S., Madaah Hosseini, H.R., Dolati, A.: The effect of cationic and anionic surfactants on the nanostructure and magnetic properties of yttrium iron garnet (YIG) synthesized by a sol-gel

auto combustion method. Russ. J. Non-Ferr. Met. **53**(4), 308–314 (2012)
34. Rashad, M.M., Hessien, M.M., El-Midany, A., Ibrahim, I.A.: Effect of synthesis conditions on the preparation of YIG powders via co-precipitation method. J. Magn. Magn. Mater. **321**(22), 3752–3757 (2009)
35. Zhan Xing, S., Fang, M.H., Chen, D.H., Wei, L.X., Liu, Y.G., Huang, Z.H.: Synthesis of YIG nanopowders by sol-gel method, Trans Tech Publications Ltd. In Key Eng Mater. **368**, 582–584
36. Yu, H., Zeng, L., Chao, Lu., Zhang, W., Guangliang, Xu.: Synthesis of nanocrystalline yttrium iron garnet by low temperature solid state reaction. Mater. Charact. **62**(4), 378–381 (2011)
37. Anand, S., Pauline, S.: Electromagnetic interference shielding properties of $BaCo_2Fe_{16}O_{27}$ nanoplatelets and RGO reinforced PVDF polymer composite flexible films. Adv. Mater. Interfaces **8**(3), 2001810 (2021)
38. Anand, S., Pauline, S.: C Joseph Prabagar, Zr doped Barium hexaferrite nanoplatelets and RGO fillers embedded polyvinylidenefluoride composite films for electromagnetic interference shielding applications. Polym. Testing **86**, 106504 (2020)
39. Yu, Y.: Ling Yu, Kaimin Shih, and. J. Paul Chen, Yttrium-doped iron oxide magnetic adsorbent for enhancement in arsenic removal and ease in separation after applications, Journal of colloid and interface science **521**, 252–260 (2018)
40. Santhosh, C., Kollu, P., Felix, S., Velmurugan, V.: Soon Kwan Jeong, and Andrews Nirmala Grace, $CoFe_2O_4$ and $NiFe_2O_4$@ graphene adsorbents for heavy metal ions–kinetic and thermodynamic analysis. RSC Adv. **5**(37), 28965–28972 (2015)
41. Emami, S., Madaah Hosseini, H.R., Dolati, A.: The effect of cationic and anionic surfactants on the nanostructure and magnetic properties of Yttrium Iron Garnet (YIG) synthesized by a sol-gel auto combustion method. Russ. J. Non-Ferr. Met. **53**(4), 308–314 (2012)